

## Finite Element Method Simulation of the Field Distribution for AFM Tip-Enhanced Surface-Enhanced Raman Scanning Microscopy

Miodrag Micic, Nicholas Klymyshyn, Yung Doug Suh, and H. Peter Lu\*

Pacific Northwest National Laboratory, Fundamental Science Division, P.O. Box 999,  
Richland, Washington 99352

Received: September 12, 2002; In Final Form: December 3, 2002

Electric field enhancement distributions encountered in atomic force microscopy (AFM) tip-enhanced surface-enhanced Raman spectroscopy (SERS) experiments (AFM-SERS) are simulated using a frequency-domain three-dimensional finite element method to solve Maxwell's equations of electric field distributions. We simulated an electromagnetic field enhancement in the vicinity of an AFM tip in close proximity to silver spherical nanoparticles under the illumination of a laser beam of various incident angles under different geometric arrangements. Maximum electric field enhancement is discussed in terms of the relative position of the tip and nanoparticles, as well as the direction of excitation laser propagation. Our results suggest new approaches for using AFM-SERS tip-enhanced near-field technique to image samples on surfaces.

### Introduction

Although scanning probe techniques, such as AFM<sup>1</sup>, scanning confocal microscopy,<sup>2,3</sup> and derived techniques, have significantly advanced the way we look at the topography of surfaces at the nanoscale, the drawback of those techniques has been the lack of chemical identification of observed features. One of the most promising techniques for obtaining nanoscale chemical mapping and composition characterization is to combine AFM with surface-enhanced Raman spectroscopy (SERS) into a single experiment (AFM-SERS). In this procedure, the spectroscopic and topographic identification may be obtained from the Raman spectra at the nanoscale of AFM spatial resolution. Such Raman signals can be significantly enhanced by the antenna effect at near-field, combined with surface plasmon enhancement induced by a metallic AFM tip close to an explored sample. In the macroscopic technique of SERS, which has been known for almost three decades,<sup>4</sup> the Raman signal enhancement occurs when the investigated molecules are adsorbed onto the rough metallic electrode surface and the colloidal nanoparticles.<sup>4–6</sup> More recently, the combination of AFM and SERS techniques has been demonstrated by several independent research groups,<sup>7–10</sup> opening tremendous opportunity for chemically specific scanning probe microscopy. These methods will have the most significant impact on biological and chemical-specific imaging, with the possibility of *in situ* single-molecule studies<sup>6</sup> and chemical mapping of the environment at the cellular membrane of living cells or of individual crystalline grains in geological or environmental samples. However, performing good-quality Raman imaging at nanoscale size, with high contrast and good signal-to-noise ratio, represents a significant challenge. It is necessary to determine optimal geometric configurations (the arrangement of the metallic AFM tip, samples, and nanoparticles) of the local field enhancers and the incoming excitation beam to achieve the highest possible local electric field ( $E$ ) enhancement confined in the smallest spatial volume. As the Raman signal intensity is proportional to the  $E^4$ , small variations in the electric field intensity will induce dramatic changes in

the Raman signal.<sup>4a</sup> The critical parameters for the optimal conditions to achieve maximum field enhancement are the configuration among the tip, nanoparticles, and laser excitation beam. It is a complex task to optimize these parameters experimentally because it requires various geometric arrangements of the tip over the nanoparticles and the incoming laser beam with appropriate polarization. Therefore, it is desirable to simulate the electric field distribution by solving the system of Maxwell's equations for different geometric arrangements, in searching for the optimal experimental configurations. Our numerical simulation to model different geometric configurations of the maximal electric field enhancement will complement our group's<sup>10</sup> and other groups'<sup>7–9</sup> experimental developments of AFM-SERS techniques. Results will allow us to plan AFM-SERS experiments precisely, especially in complex media, for example, in the vicinity of the environment of cell membranes.

This paper presents the results of a numerical simulation of electric-field enhancement in the configurations comprising the Ag AFM tip and Ag nanoparticles in their vicinity within the near-field range. The described model is based on Maxwell's equations, and the surface plasmon effect is therein treated indirectly through an adequate selection of complex material dielectric constants. The Maxwell-equation-based models do not handle any other specific chemical enhancement effects. However, as both the surface plasmon and chemical enhancement act as leverage-multipliers of the electric-field enhancement, our approach in solving the electric-field distribution in the AFM-SERS simulations provides valuable insights (e.g., into the location and shape of the field-enhanced region) to the ultimate spectroscopic and spatial resolution of AFM-SERS microscopy, and identifies the best geometric configuration (arrangement of tip, samples, and nanoparticles) to produce the highest field enhancement.

First, we compare the results from our frequency-domain FEM simulation with the previous finite-difference time-domain (FDTD) method,<sup>11,12</sup> multiple multipole method (MMP),<sup>13</sup> and time-domain finite-element method<sup>14</sup> for a benchmark system, consisting of a single Au tip. This simulation involves field enhancement from a plain Au tip illuminated by a laser plane-

\* To whom correspondence should be addressed. E-mail: peter.lu@pnl.gov.

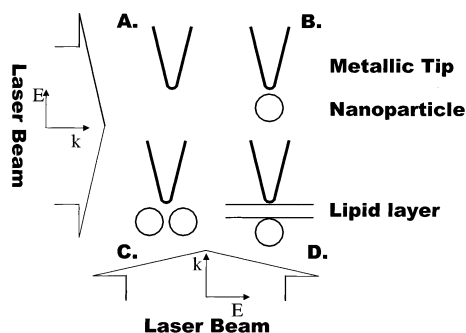


**Figure 1.** Schematic representation of the simulated configurations of AFM-SERS experiments: (a) Au AFM tip with no particles present; (b) Ag AFM tip in vicinity of the single Ag nanoparticle; (c) Ag AFM tip in vicinity of two geminal Ag nanoparticles; (d) Ag AFM tip positioned above particle embedded under the lipid layer. All configurations were simulated with the laser beam propagating under incident angles, ranging from horizontal to vertical. Notations  $\mathbf{k}$  and  $\mathbf{E}$  represent the laser beam propagation vector and laser electric field vector, respectively.

wave, propagating from the bottom and side (Figure 1a). Next, we simulate the field enhancement in the vicinity of an Ag tip in the presence of Ag nanoparticles (Figure 1b–d). The influence of relative distances is then simulated between the tip and a single nanoparticle or pair of nanoparticles and between a pair of nanoparticles, as is the influence of different laser beam propagation directions and different tip shapes/sharpness. Finally, we present the optimum geometric arrangement of all constituents for achieving maximal field enhancement.

## Models and Methods

To solve Maxwell's equations in the short-field approximation, we use the frequency-domain finite element method (FEM). As a general way to solve the partial-differential equations of the general potential theory problems, by a peculiar application of variational methods, the FEM method was first introduced by Courant<sup>15</sup> in 1943. Approximating a limited domain by linear approximation with a set of triangles (the elements), Courant solved an example of the partial differential equation, which provided the foundation of what later was referred to as FEM. Silvester<sup>16</sup> presented the first application of FEM for solving the electromagnetic field problem based on Maxwell's equation. Recently, there has been significant progress toward FEM applications in optics, optical engineering, and nanotechnology.<sup>17,18</sup> Here, we use FEM with a frequency-domain approach and a fully enclosing three-dimensional mesh, based on the tetrahedral (first order) elements to simulate the near-field problem of tip and nanoparticle-induced local electric-field enhancement in an AFM-SERS experiment. Four different geometric configurations (Figure 1a–d) are modeled, corresponding to realistic AFM-SERS scenarios. Figure 1a represents a single Au AFM tip, submerged in an aqueous medium, whereas the Figure 1b,c represent a Ag tip with similar geometry in the vicinity of a single Ag or Au nanoparticle and a pair of nanoparticles. Figure 1d depicts a configuration of the biological membrane layer between the metallic tip and a nanoparticle. All of the calculated results are obtained with a three-dimensional FEM simulation. The dielectric constants, which depend on the material and the excitation laser wavelength, are assumed to be uniform within the boundaries of the metallic tip and nanoparticles. In Figure 1a, the configuration is modeled with a full 360° mesh to investigate an asymmetric field enhancement. The same metallic tip shape, i.e., 10° tip divergence and 5-nm-radius tip curvature, and the unity laser

excitation field are used in the simulations. The laser beam has been represented as a plane-wave, due to the significantly larger size of the beam (approximately a few hundred nanometers) in the experimental conditions compared with the size of the configuration modeled. The material dielectric constants have been taken from previous publications dealing with simulations of field enhancements in near-field microscopy<sup>11–14</sup> and measurements of thin-film optical properties.<sup>19</sup> In our simulation, the far-field radiation boundary was modeled using the surface impedance ( $Z$ ) boundary condition of  $Z = (\omega_0/\epsilon_0)^{1/2}$ , wherein the  $\omega_0$  is the permeability of free space and  $\epsilon_0$  is the free-space permittivity. The solver used in this work is the ANSYS solver with the Multiphysics add-on for solving near-field and high-frequency problems.<sup>20</sup>

In principle, both frequency-domain and time-domain FEM calculations give the same results in solving Maxwell's equations. Frequency-domain FEM calculations are the current state-of-the-art in electromagnetic FEM solvers although they require significantly more computational power compared to time-domain FEM. Due to large computational requirements, frequency-domain FEM solvers have become readily available only recently.

To solve a high-frequency electromagnetic problem, a complete set of Maxwell's equations must be used, and the displacement current in Maxwell's equations must be considered. In the FEM model, a closed surface separates the finite mesh volume of numerical integration from the infinite open domain. An electromagnetic plane-wave is projected to the finite numerical domain to represent an incident laser beam. The geometric scenery is modeled by shaping the mesh in the form of the configuration, positioning radiation sources and material inhomogeneity within the elements of the mesh of the finite numerical volume. The Maxwell equation in ANSYS is presented in the vector notation well-known as a Helmholtz equation.<sup>20</sup> The total electric field vector is approximated as a linear sum of products of vector basis function and projection of the vectors of the electric field at the edge, face, or volume of the element. The weak formulation of the Helmholtz equation is presented in the matrix notation, which is suitable for numerical integration,<sup>20</sup> and represents the core of the Ansys Multiphysics solver.

In our particular case, for the volume discretization, we used a first-order tetrahedral element. It is the simplest three-dimensional shape, capable of modeling any geometric form, and is very suitable for the automatic mesh generation. Moreover, in the case of geometric configurations involving oval objects, the oval shapes can be best modeled using a dense mesh composed of this element (Figure 2a). The first-order element is very versatile in creating complex meshes, requiring less expensive computation than the more complex elements of the higher orders. Second-order elements were tested in this situation and proved to increase computation time without significantly affecting the results. We used this element in the form of a tangential vector element, i.e., an element for which the degrees of freedom are not associated with the particular nodes but with entities of higher dimensionality, such as edges, faces, and volumes. Using such an approach, it was possible to avoid a plethora of problems of calculating a field in a node-based element, especially where there are near-field and high-frequency problems. The vector element did not require specific treatment of the dielectric constant and special boundary conditions at the interfaces of two different materials, as opposed to the case of using the node elements. Furthermore, tangential vector elements did not have problems with ambiguous electric

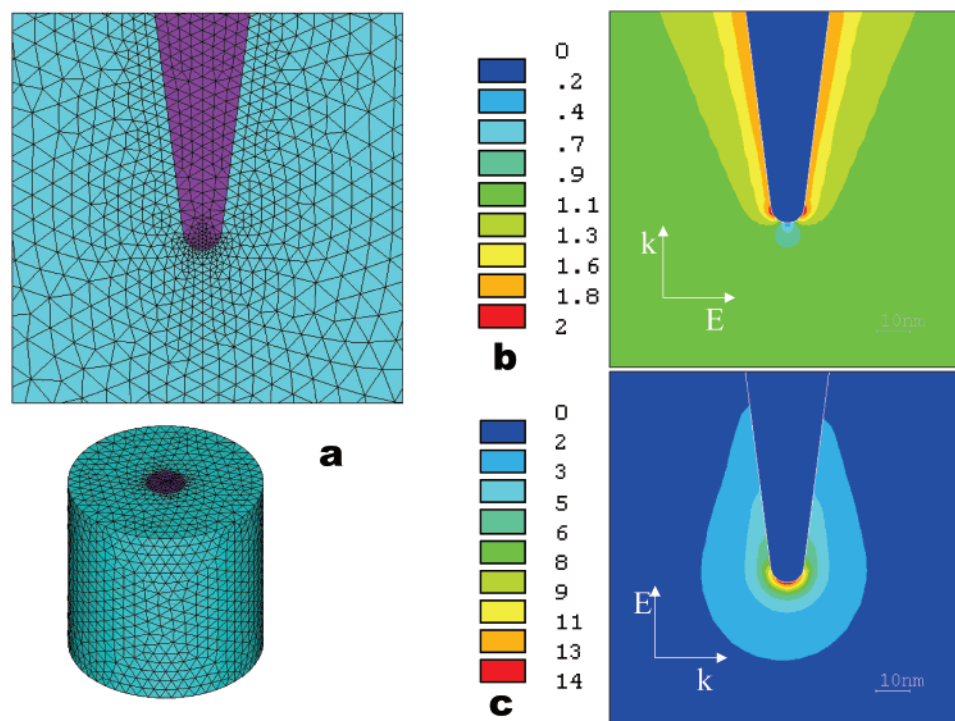


**Figure 2.** Field enhancement in the vicinity of the Au AFM tip under the plane-wave laser illumination at 810 nm: (a) complete 3D mesh and the cross-section of the FEM model; (b) electric field distribution around the AFM tip irradiated from the bottom (central cross-section of the 3D model); (c) electric field distribution around the AFM tip irradiated sideways (central cross-section of the 3D model).

fields due to point-irradiation problems, as in the case of the node-based elements. Under our applied first-order tetrahedral element, the tangential component of the electric field was constant along the edge, and the normal component was variable.

Finite-element meshes used for all of the simulations presented here were automatically generated using the ANSYS preprocessor software package.<sup>20</sup> The mesh density, especially in the vicinity of interfaces, was kept to at least 10 elements per wavelength, thus securing the converged electric field solutions. The mesh density was increased in the area of high curvatures, and in the interfacial areas. In our simulation, the saturation condition of the mesh density was carefully evaluated and reached to ensure the simulation accuracy.

## Results and Discussion

**I. Electric Field Enhancement in the Vicinity of the Metallic AFM Tip: Testing the Validity of Our Frequency-Domain FEM Simulation Model.** In the first case, a free metallic Au tip in an aqueous environment was irradiated using axial and perpendicular laser wave propagation. This case was used as a benchmark test to validate our approach. The geometric details and material constants were the same as those in the near-field tip-induced enhancement reported in the literature.<sup>11–14,19</sup> We sought to validate our frequency-domain FEM approach by examining the field distributions and absolute calculated intensities of the electric field in such simulations. The model consisted of the gold tip ( $\epsilon = -24.9 + 1.57i$ ) with radius of an apex of 5 nm immersed in an aqueous environment ( $\epsilon = 1.77$ ) and irradiated with the plane monochromatic wave at  $\lambda = 810$  nm. The selected wavelength was not only optimal for the resonance conditions, but in the experimental setup, use of such a long wavelength eliminated the problems associated with inducing fluorescence. Two different configurations were analyzed with beam propagation being orthogonal with the tip axes and parallel to the tip axes. The information sought from this simulation was the electric field enhancement defined as a

ratio of the total to the incoming electric field intensities,  $M = |E_{\text{tot}}/E_0|$ . Keeping the intensity of the electric field of the incoming laser beam ( $E_0$ ) to 1, we can consider the calculated electric field, scalar intensity  $E_{\text{tot}}$ , as numerically equivalent to the enhancement  $M$ . Figure 2a depicts the finite element three-dimensional mesh of the tip immersed in an aqueous media. Parts b and c of Figure 2 represent solutions of a near-field problem with the laser beam propagating from the bottom (Figure 2b) and side (Figure 2c), i.e., having the propagation vector  $\mathbf{k}$  oriented vertically (Figure 2b) and horizontally. Consequently, the incoming electric field vector  $\mathbf{E}$  is orthogonal and oriented horizontally (Figure 2b) and vertically (Figure 2c). Our simulated field is found to be in good agreement with the results of the field distribution<sup>11–14</sup> and the field-enhancement intensity,<sup>11,12,14</sup> calculated using the time-domain FEM method,<sup>14</sup> multiple multipole method,<sup>13</sup> and the finite-difference time-domain method (FDTD).<sup>11,12</sup> Therefore, we confirm the usefulness and viability of using the frequency-domain FEM solver in solving the nanoscale electric field distribution problems.

We obtained a maximum electric field enhancement of 2 and 14 for the vertical and side illumination of the tip, respectively. However, the electric field enhancement due to the antenna effect, simulated by solving Maxwell's equations, is just the first part of the picture. The localized electric field interacts with molecules adsorbed at the metallic surface—media interfaces, induces surface plasmon resonance, and interacts with molecules through electronic coupling (chemical enhancement), which are all neglected by the basic antenna-effect calculations. The surface plasmon resonance is accounted for implicitly through the wavelength-dependent materials dielectric constant. There is no other explicit analytical characterization of the enhancements due to the surface plasmon and chemical interactions in this simulation. Nevertheless, it is well-known that the intensity of the Raman signal is in a fourth power ( $E^4$ ) relationship with the electric field in the vicinity of the molecules. Thus, each of the above-described effects acts as a



leverage factor in the final Raman signal enhancement, so that the results of this kind of simulation can be used to find the most optimal AFM-SERS experimental conditions and justify proposed experimental configurations.

**II. Electric Field Enhancement in the Single Nanoparticle–AFM Tip Configuration.** One of our main interests is to study antenna contributions to the field enhancements in response to the relative position of the AFM tip over a single metallic nanoparticle. In this case, a Ag metallic tip, with the same geometry as the previous case, was positioned above the sphere, representing a Ag nanoparticle with a diameter of 80 nm. The material constant was based on the one used for Ag,<sup>19</sup>  $\epsilon = -32.8 + 0.458i$ , with a laser beam wavelength of  $\lambda = 810$  nm. The surrounding environment was modeled with  $\epsilon_o = 1 + 1i$  constant, to achieve the maximum transparency for the incoming laser beam and to avoid dumping field attenuation artifacts, which would result from signal attenuation before reaching the tip and/or nanoparticles. The obtained electric field distribution was thus generated entirely by the constituents of the experimental setup. In reality, with water surroundings<sup>13</sup> ( $\epsilon = 1.77$ ), we could expect slight distance-dependent attenuation of the incoming laser beam and slightly lower absolute values of the local electric field enhancement. However, in a living cell, the medium is much more complex than in a homogeneous vacuum or water. Thus, for exact modeling of the field distribution within cell structures, it is necessary to obtain more experimental data on permeability and permittivity of the different cell constituents and on the cytoplasm media.

*(1) AFM Metallic Tip Near-Field Enhancement Using 80 nm Ag Nanoparticles and the Different Mode at Different Excitation Laser Orientation.* Parts a–b of Figure 3 represent the field distribution in a configuration comprising a single 80-nm particle with the tip positioned above the nanoparticle. Figure 3a represents the distribution of the electric field enhancement with laser light illuminating from the bottom, i.e., with a vertical propagation vector, whereas Figure 3b represents the case of sideways illumination, i.e., a horizontal laser propagation vector. For sideways illumination, a high field enhancement can be observed in Figure 3b between the tip and the nanoparticle, confined within a volume with radius less than the radius of the tip apex.

Of practical interest is also vertical illumination (Figure 3a), in which the maximum enhancement is not achieved between the tip and nanoparticle but on the side of the irradiated nanoparticle. The enhancement volume has a 10- to 20-nm diameter for a 80-nm nanoparticle and is positioned sideways, in asymmetric form around the nanoparticle. Although the intensity of such an enhancement is an order of magnitude smaller than that for the interstitial site between the nanoparticle and the tip for a horizontally illuminated configuration (Figure 3b), the 3.0 factor of the field enhancement can presumably give an  $\sim 80$ -fold enhancement of the Raman scattering signal because the Raman signal is proportional to the fourth power of the field. Those facts are of special importance for possible biological application of the AFM-SERS method. Sideways electric field enhancement (Figure 3a) will enable selective, direction-sensitive Raman studies of cell membrane structures *in vivo*.

*(2) AFM Metallic Tip Near-Field Enhancement of Using the 10 nm Ag Nanoparticles and the Tip–Particle Separation Distance Dependence.* For Raman imaging at cell membranes, it is also very interesting to examine the behavior of the smaller nanoparticles, common for the immuno-gold-based and immuno-

silver-based labeling.<sup>21</sup> Small metallic nanoparticles can be used as optical single-molecule labels that possess advantages over organic dye molecules and semiconductor nanoparticles because of the stability they exhibit in photobleaching and photoinduced emission blinking.<sup>22</sup> Such nanoparticles, when attached to the appropriate antibodies, are usually 5–10 nm in diameter.<sup>21,22</sup> It is very interesting that our simulation suggests that a strong electric field enhancement occurs between the nanoparticle and tip even if such a small nanoparticle should theoretically be much off the peak surface plasmon resonance wavelength of 810 nm.

In biological imaging, virtually any applied method must be capable of studying different parts of cell structures, especially membranes, which could be located anywhere within the cell volume. Thus, we examined the tip–particle distance relative to the observed electric field enhancement intensity and shape of the corresponding volume. Parts c–f of Figure 3 represent the tip in the vicinity of 10-nm nanoparticles at various particle–tip distances. In the case presented in Figure 3c, there is no separation between the nanoparticle and the tip; i.e., the tip touches the nanoparticle. In such a configuration, the nanoparticle essentially plays a role in virtual tip extension, and the distribution of the electric field enhancement is essentially the same as in the case of single tip. The maximal electric field enhancement is located at the bottom of the nanoparticle, and in this particular configuration the calculated intensity of the field enhancement is 24. Increasing the distance between the tip and the particle (Figure 3d), electric field enhancement initially increases, with relocation of the volume of maximal electric field enhancement to the geometric position between the tip and the nanoparticle. With a further increase in tip–particle distance (Figure 3e), the maximum electric field enhancement is separated into two different domains, with the domain of the highest field being in front of the tip and the domain with a somewhat lower electric field enhancement being located at the particle. This effect could be best depicted on the series of figures representing electric field enhancement at various tip–particle distances from 0 to 15 nm (Figure 3c–f). It is obvious that, in this case, the volume of maximum field enhancement is uniformly spread between the tip and nanoparticle. With a further increase in the particle–tip distance, we can spot a separation of electric field enhancement into two components, one induced by the nanoparticle and another by the tip. For example, Figure 3e represents the electric field in the vicinity of the tip and a 10-nm nanoparticle when the tip–particle distance is increased to 3 nm. In this case, it is clearer that the maximum field enhancement obtained is actually composed of the sum of two superimposed local electric field enhancements, one being the local field of the nanoparticle and another being that of the tip. The field gradient in such a case points toward the tip. With further separation, e.g., of 15 nm as shown in the Figure 3f, two completely separated domains can be observed that contain an enhanced electric field, the stronger domain being in the vicinity of the tip and the lesser in the vicinity of the nanoparticle. We conclude, then, that the influence of the tip on the molecules in the vicinity of the surface on the nanoparticles is negligible. To be able to exploit the maximal field enhancement, and thereby the best signal-to-noise ratio in a tip-enhanced AFM-SERS experiment, the distance between the tip and metallic nanoparticles must be kept in the range of optimal enhancement, e.g., for 10-nm nanoparticles, that range is 1–5 nm.

Figure 3g, curve A, plots the maximum field enhancement against the small particle–tip distance, with a horizontal laser

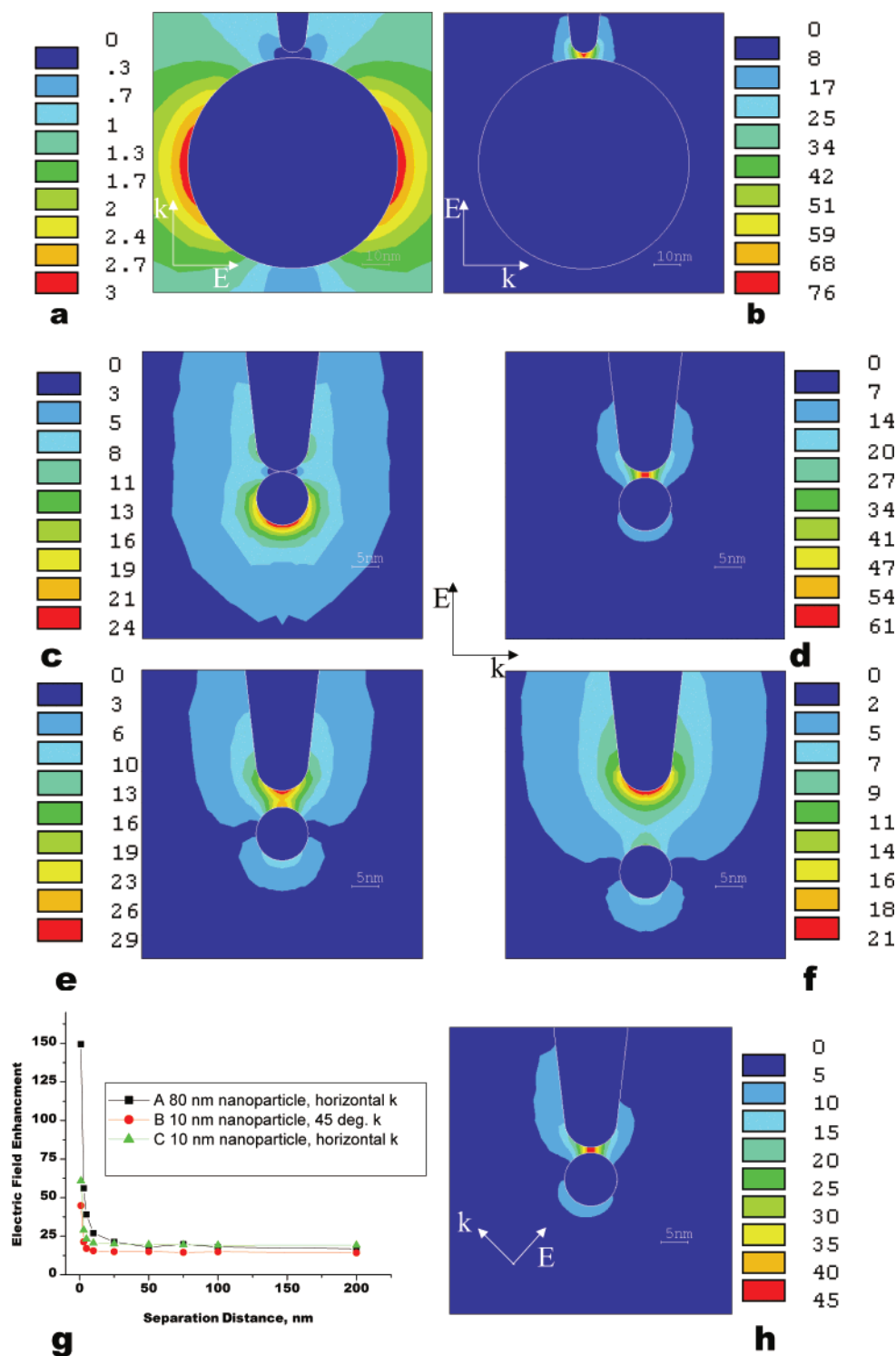


**Figure 3.** Field enhancement in vicinity of the Ag AFM tip positioned above the single Ag nanoparticle under the laser illumination at 810 nm (central cross-section of the 3D model): (a) electric field distribution in the case of the large nanoparticle (80 nm) irradiated with laser light coming from the bottom (particle–tip separation distance 2 nm); (b) electric field distribution in the case of the large nanoparticle (80 nm) irradiated with the configuration irradiated sideways (particle–tip separation distance 2 nm); (c)–(f) electric field distribution in the case of the tip positioned above the small nanoparticles (10 nm) illuminated sideways at various separation distances (c, 0; d, 1; e, 3; f, 15 nm); (g) graphical representation of dependence of the field enhancement of configuration (c) on tip–particle distance; (h) electric field distribution around the 10-nm nanoparticle in the tip vicinity illuminated with the laser beam under the incident angle of 45°.

beam propagation vector (vertical  $\mathbf{E}$  field). However, in microscopic optical imaging, when using a high numerical-aperture objective to have diffraction-limited focus of the excitation light, the laser beam typically contains a finite divergence propagation angle rather than a purely horizontal or vertical one. We have simulated the same geometric configuration of the small particle and tip under a different

excitation-laser propagation angle. Curve B of Figure 3g shows the results of separating the tip from a 10-nm nanoparticle, with the incoming laser propagation vector at 45° from vertical (Figure 3h). The dependence of the enhancement on the change in separation distance is essentially the same as that for the horizontal laser beam propagation (vertical  $\mathbf{E}$  field), except that the absolute value of the field intensity is lower.

Figure 3h shows the 1 nm separation of the tip and a 10 nm nanoparticle with the incoming laser propagation vector at  $45^\circ$ . Compared to the horizontal beam propagation of Figure 3d, the only change in the field enhancement is a slight electric-field asymmetry although the volumes of maximum enhancement remain essentially the same. This result indicates (a) that the configuration of the tip in the vicinity of a small nanoparticle can be a viable probe in studying a biological system and (b) that it will not be prone to the divergence of the laser propagation angle. This is experimentally significant because the divergence may occur due to experimental constraints, such as microscope objective focusing, misalignment, or light-scattering within a medium.

(3) *Near-Field Enhancement is Similar Regardless of Particle Size.* Figure 3g, curve A, represents the results of the simulation of spreading a larger particle, 80 nm in diameter, and the tip with sideways illumination (vertical **E** field). Curve A shows almost the same distance dependence as curves B and C, except for the higher intensity of the field enhancement and the more sensitive dependence of the enhancement versus tip position. It is interesting that the spatial resolution, comparing with the configuration involving a 10-nm particle and a 80-nm particle, remains the same; i.e., the volume of maximal electric field enhancement is within the same size range. This result indicates that the AFM-SERS imaging spatial resolution and Raman signal will not fluctuate due to possible inhomogeneous sizes of the nanoparticles used in the imaging experiments.

(4) *AFM Metallic Tip Locks the Modes of the Near-Field Enhancement Distribution.* For the purpose of studying biological structures, it will be very convenient to use configurations with only one nanoparticle, irradiated from below, because the volume of maximal excitation is formed not between the AFM tip and nanoparticles but sideways on the nanoparticle, thus allowing the surfaces of biological structures (e.g., cells or vesicles) to be probed through close proximity to the nanoparticle. It has been demonstrated in immunologic imaging that gold nanoparticles can be tethered with antibody proteins that can selectively bind to the target biological components inside the living cells, as well as to the interfacial structures.<sup>21,23</sup> It was shown recently that colloidal gold labeling within the living single cell has promise for in vivo intracellular Raman spectroscopy.<sup>23</sup> AFM-SERS utilizing immunologically labeled metallic nanoparticles will be powerful in imaging targeted components and molecules in living cells, particularly at cellular membranes.

The influence of the tip position relative to the intensity and shape of the enhancement volume was estimated for the bottom-irradiated configuration, comprising a single, larger Ag nanoparticle (80 nm in diameter) and tip. Simulations were performed for different positions of the tip relative to the nanoparticle (see, for example, Figure 3a), with the tip positioned above the nanoparticle and moved from direct contact up to a 10-nm separation (data not shown). Slight differences in electric field enhancement were observed between two configurations: (a) a single nanoparticle and (b) a tip and a nanoparticle, irradiated from the bottom. Simulating a single particle without the tip, an electric enhancement of about 3 was obtained, thereby indicating that in this configuration, the tip does not have a significant enhancement effect and that the position of the field enhancement is determined solely by the direction of the laser wave propagation. However, the tip plays an important role in polarizing and locking the electric field distribution around the particles. Especially in the case of particles with spherical symmetry, the tip breaks the symmetry of the electric field

distribution, from spherical to axial. Its presence polarizes the particle and geometrically constrains the volume of the maximum electric field enhancement, creating, in the case of vertical and horizontal beam propagations, completely different field distributions around the particles. However, achieving absolute sideways beam propagation is inconvenient, if not virtually impossible, in a real imaging microscopic experiment. The beam propagation will always be somewhere between horizontal and vertical due to focusing of the beam with the microscope objective. Therefore, locking the enhancement mode by the tip is important to avoid the excitation-field direction fluctuations that result from light scattering by the complex sample structure, such as the complex dielectric components in living cells.

(5) *Excitation Laser Beam Propagation Angle Dependence.* Figure 4a shows the angular dependence of the intensity of electric field enhancement for a single particle with the tip positioned above. Enhancement saturation occurs when the angle of laser beam propagation approaches horizontal (Figure 4a). The shapes of the field distribution around the single 80-nm particle at various angles are presented in Figure 4b–d. It is interesting that the field enhancement always occurs either in the space between the AFM tip and the nanoparticle, if beam propagation is closer to the horizontal, or on the particle sideways, if the beam propagation is closer to the vertical. There is no intermediate mode of electric field enhancement observed, which confirms (a) that the presence of the tip polarizes the electric field enhancement and (b) that, in the presented geometric configurations, two favorable modes exist, one where the “knot” of enhancement occurs between the nanoparticle and the tip, and the other where the enhancement occurs on the side of the tip. It is most likely that this effect has its origin in the elongated shape of the tip.

(6) *Tip Apex Divergence Angle Dependence.* There are not only various sizes of nanoparticles that could be used in different experimental setups but also tips of various sizes of apex. Therefore, we modeled the influence of the tip size on the field enhancement, varying the tip apex angle from  $0^\circ$  to  $180^\circ$ , within a configuration consisting of the tip positioned 1 nm above single nanoparticle (80 nm in diameter). The resulting distributions of the electric field for representing angles are presented in the Figure 5a–e, whereas the dependence curve of the field enhancement on the tip apex angle is shown in the Figure 5f. Initially, with the increase of the tip apex angle, there is an increase in the intensity of the electric field enhancement. However, the total variation of the electric field enhancement remains relatively small, about 30% within the range of applied angles from  $0^\circ$  to  $120^\circ$ . Thus, for the purposes of AFM-SERS imaging and single-molecule spectroscopy, no significant gain on the field enhancement will be obtained by using very sophisticated and expensive, ultrasharp, or specially shaped tips, e.g., focus ion-milled, whiskers, or nanotube tips. The AFM metallic tips with a broad range of tip apex angle will perform adequately. However, an ultrasharp tip does have an advantage in the limited cases of high spatial resolutions and when a specially shaped tip would be necessary to access a place of the interest. It is also interesting that cylindrical tips with flat bottoms (essentially representing  $180^\circ$  of an apex cone, as depicted on the Figure 5e) will still produce a field enhancement but with only about one-third of the intensity of the conical tips.

**III. Electric Field Enhancement in the Configuration of Two Geminal Nanoparticles and AFM Tip.** Recently, it has been reported<sup>5,6,10</sup> that a large Raman enhancement could be obtained from a single molecule or molecules positioned at the

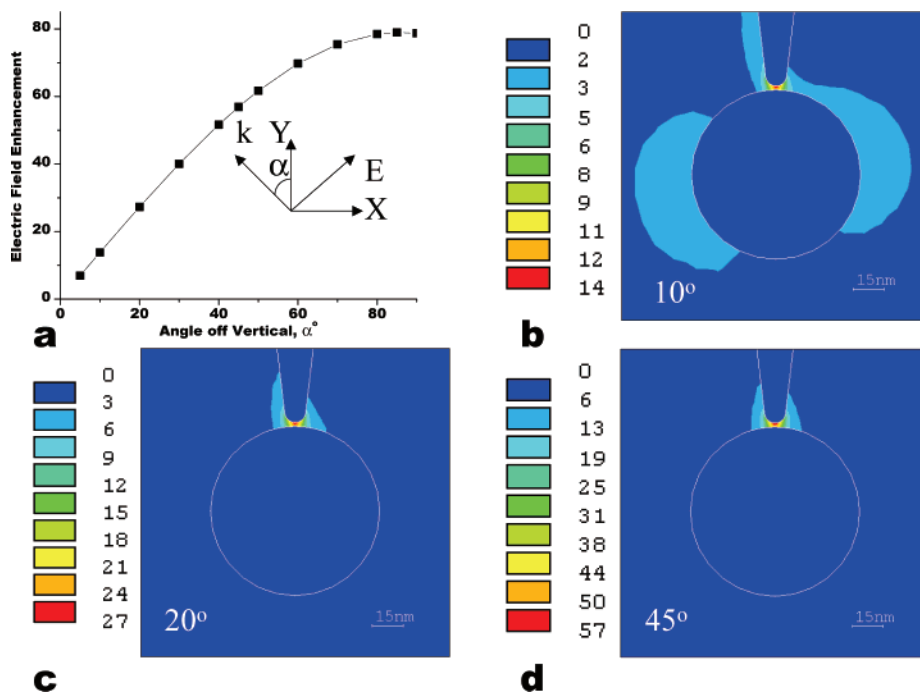


**Figure 4.** Angular dependence of the electric field enhancement in the case of the Ag tip over single Ag nanoparticles (central cross-section of the 3D model): (a) diagram of E-field enhancement vs angle of laser beam propagation; (b)–(d) shape of electric field, under different incident angles of incoming laser beam (b, 10°; c, 20°; d, 45°).

interstitial site of a pair of nanoparticles. We simulated an AFM metallic tip positioned above the juncture of a pair of Ag 80-nm nanoparticles, with the laser beam propagating either vertically (Figure 6a) or at 45° (Figure 6b). Figure 6 shows the electric field in the local area around the maximum field enhancement at the interstitial site. In the case of a laser beam with vertical propagation, the calculated field enhancement is highest in the interstitial site between the pair of nanoparticles, and the field enhancement volume is somewhat smaller and more concentrated than that of a single particle–tip configuration under either horizontal or vertical excitation beam directions. Due to such a favorable field enhancement, a further study of this configuration has been performed. Figure 6c, curve A, summarizes the field-enhancement simulation of different positions of the AFM tip relative to a pair of nanoparticles. In this simulation, the tip was moved vertically, from touching the particles to 200 nm above the particles. Curve A shows that when the excitation laser beam propagates vertically (horizontal  $\mathbf{E}$  field), the field enhancement is almost the same, with or without the tip present; i.e., no significant tip influence on the field enhancement has been observed in this configuration. In contrast, at a particular distance between the tip and the pair of nanoparticles when the excitation laser illuminates with a 45° angle (propagation vector  $\mathbf{k}$ ) (Figure 6b), an additional center of electric field enhancement is formed, located between the particles. In this configuration, the field enhancement between particles remains the same intensity as the tip–particle separation distance changes. However, the additional, lateral electric field enhancement volume exists only if the tip is in close proximity to the particles; with the increase in separation distance, it disappears completely. This effect originates in the asymmetric incoming beam excitation, which distorts the symmetry of the field enhancement around the tip apex. This effect may lead to the decrease in spatial resolution of the AFM-SERS technique, at least on the order of average distance between the two domains of high electric field enhancement. Coincidentally, the compositional, i.e., spectroscopic, resolution

can also be degraded should the two domains probe spectroscopically different chemical species.

Furthermore, FEM simulation shows that as particle separation increases, the absolute intensity of the field enhancement decreases and the enhancement volume increases. From touching to a 15-nm interstitial separation distance, the enhancement volume gradually spreads at the interstitial site. At more than about 15 nm in separation distance, the volume of the electric field enhancement splits into two separate domains and eventually reaches the same field distribution as that around a single nanoparticle. The large expansion in enhancement volume and decrease in the intensity of the enhancement indicate that with nanoparticle separation, both the spatial resolution and signal-to-noise ratio of SERS will decrease as the separation of the pair of nanoparticles increases.

The overall elongated shape of the metallic object comprising the two metallic spheres may hold the answer to the high electrical field enhancement. Recent publications<sup>6</sup> of single-molecule surface-enhanced Raman spectroscopy reported using 90-nm Ag colloidal nanoparticles and calculated the field enhancement using the boundary charged method (BCM). The results of this study were presented in the form of  $\mathbf{E}^4$  and are in good agreement with our findings presented here.

**IV. FEM Simulation of Particle Embedded under the Lipid Layer.** One of the most interesting applications of AFM-SERS is in imaging membrane proteins in living cells. In this approach, the small metallic nanoparticles are presumably located at the intracellular membrane. The most simplistic model of a proposed AFM-SERS study of membrane proteins is one comprising particles on the inside of a cell membrane, with the AFM Ag tip positioned immediately above the 2-nm-thick dielectric infinite layer ( $\epsilon = 1.96$ ), with 10-nm diameter nanoparticles positioned immediately under the same layer. The laser beam propagation vector is pointed at 45° as a realistic scenario that can be achieved using a microscope objective. The infinite layer under an aqueous environment ( $\epsilon = 1.77$ ), representing a cell wall or a membrane, has been modeled with



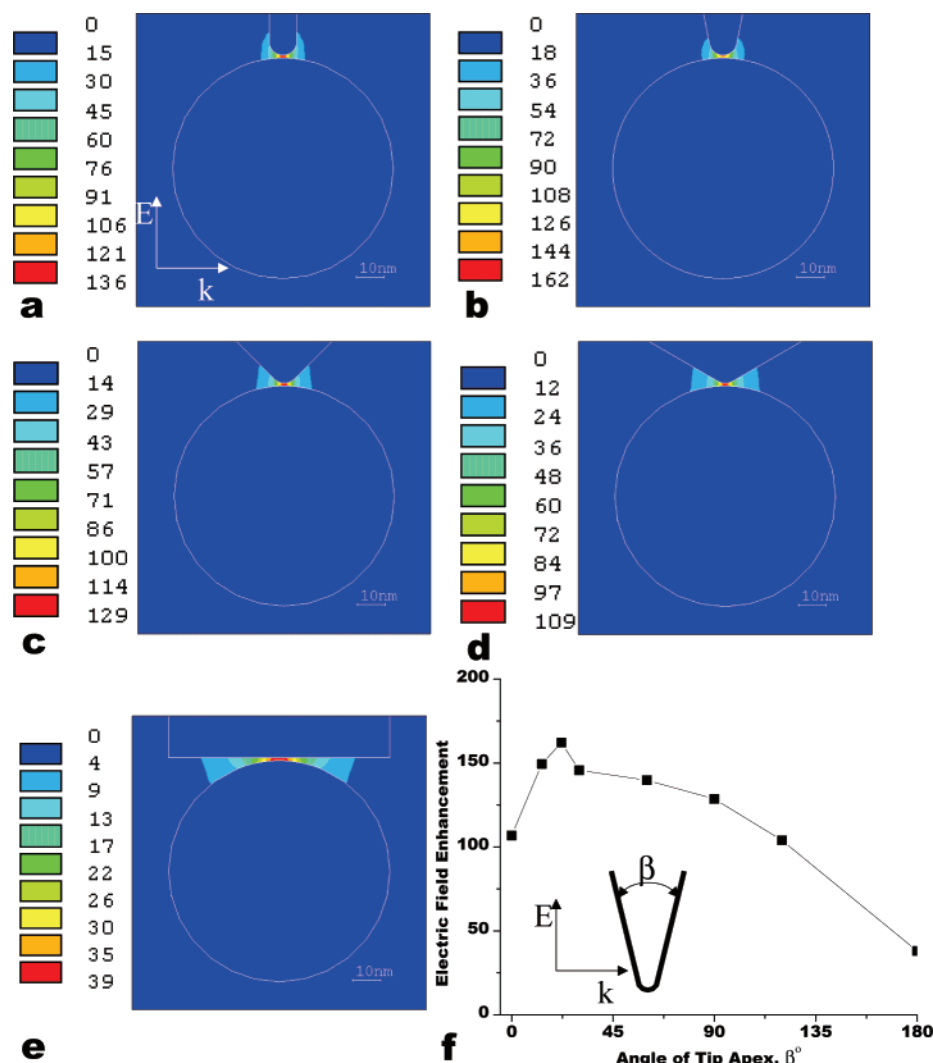


**Figure 5.** Influence of Ag tip apex angle change on the electric field enhancement (central cross-section of the 3D model). Tip is positioned on top of a 80-nm Ag nanoparticle. (a)–(e) Apex of 0° (a), 20° (b), 90° (c), 120° (d), and 180° (e). (f) Graphical representation of  $\mathbf{E}$ -field enhancement vs tip apex angle ( $\beta$ ).

the dielectric constant  $\epsilon = 1.96$ , which is typical for the hydrophobic lipid. Results of this simulation are presented in Figure 7. The electric field distribution is not as uniform as when no lipid layer is present (Figure 3h), and the volume of the electric field enhancement is spread between the tip and the particle, passing through the lipid layer. It is interesting and important, for practical applications, that the field enhancement volume is concentrated between the tip and particle, penetrating the lipid layer. This result suggests that it is feasible to label the membrane proteins with metallic nanoparticles for the purpose of selective chemical imaging and spectroscopic studies of the cell membranes *in vivo*. The volume of the enhanced electric field configured with a lipid layer is somewhat larger than that in case of the similar geometric configuration without a lipid layer (Figure 3h), and the absolute value of field enhancement is somewhat smaller. However, the field enhancement is still in the range 20–30, which would provide significant Raman signal enhancement in the range  $2 \times 10^4$  to  $8 \times 10^4$ .

**V. Limitations of the FEM Simulations and Some Possible Improvements.** Although the finite-elements method is much more versatile than the finite-difference or multiple multipole methods, there are several limitations that must be considered in analyzing simulation results. The applied methodology is based solely on the solution of Maxwell's equations, assuming that the electromagnetic field distribution is in a continuum,

“ether” space. However, because this assumption works well in the macroscopic regime, e.g., for radar antennas, lightning rods, microwave waveguides, and similar systems, one needs to be careful to estimate the feasibility of the classical electrodynamics approach for the systems at the border between the macroscopic and the quantum regime. Thus, we use FEM simulation only to calculate the electric field intensity and distributions for evaluating Raman signal enhancement, based on the simple approximation that the Raman signal is proportional to  $E^4$ . The limitations of such an approach are primarily caused by the inability to estimate the contribution of chemical enhancement to a Raman signal, and by treating of surface plasmon resonance implicitly as a macroscopic resonance through material constants.

The macroscopic electrodynamics limitation of FEM simulation makes it difficult to solve field-scattering problems from a single molecule. Although we can assume that an element much smaller than 1 nm can have a different set of dielectric constants, the results obtained will not be representative. This is because the other effects at that spatial scale, e.g., the interaction of the field with the electronic orbitals of the molecules, are much more highlighted, which is typically not the case with dimensions several tens or hundreds of nanometers larger. Furthermore, because at a very small scale the laws of quantum mechanics replace the laws of classical physics, the use of finite



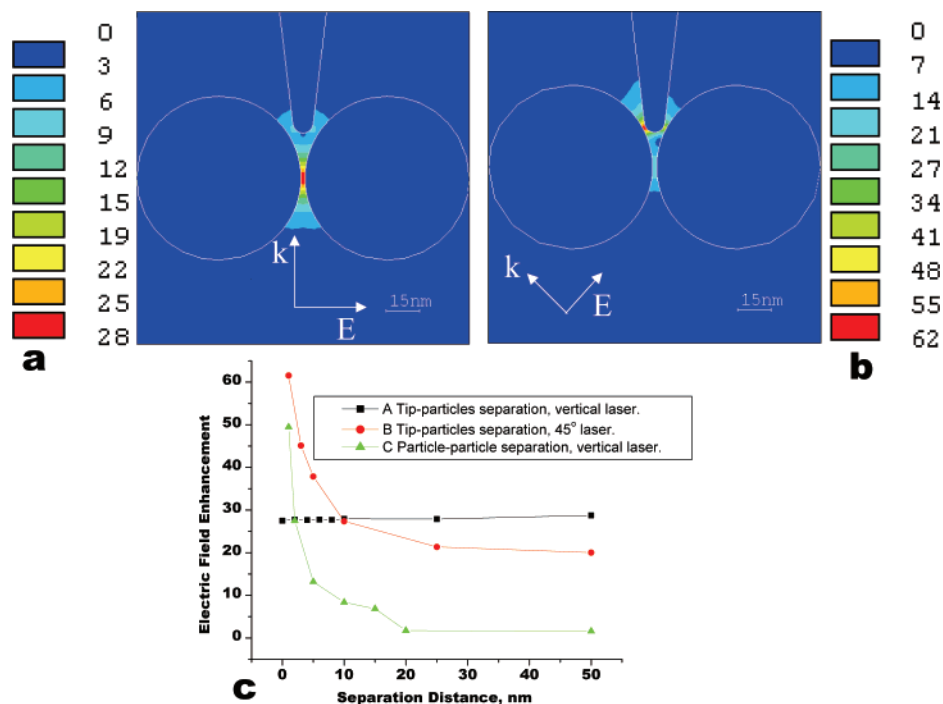


**Figure 6.** Field enhancement in vicinity of the Ag AFM tip positioned above the two geminal Ag nanoparticles under the laser illumination at 810 nm (central cross-section of the 3D model): (a) laser illumination in vertical direction; (b) laser illumination from 45°; (c) summary of field enhancement for cases (a) and (b), with changes in tip-particle and particle-particle separation distances.

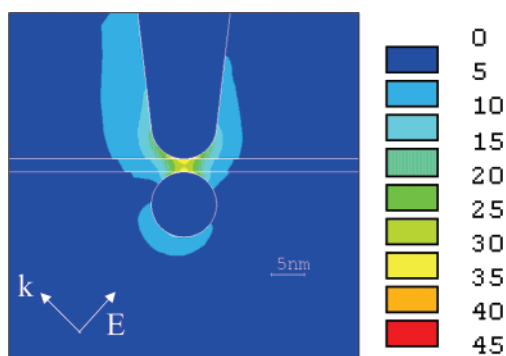


**Figure 7.** Cross-section of the configuration composed of a 10-nm Ag nanoparticle embedded under an infinite, 2-nm thick lipid membrane, with the Ag tip positioned on top of the membrane. Laser illumination at 45°.

elements and other methods of solving potential field problems are only useful up to the dimension limit of the quantum scale. For the purpose of incorporating the quantum effect into the simulation, coupling Maxwell's and Schrodinger's equations<sup>24</sup> to the theory of scanning near-field exciton microscopy<sup>25</sup> in simplified analytical form, has been reported, but a general numerical electromagnetic field modeling software based on such an approach has not yet been developed. As the electromagnetic field is responsible for many interesting effects at the size of quantum systems, an effective way of using FEM calculations in nanotechnology will be to use it to calculate electromagnetic fields at a larger scale, e.g., several tens of nanometers, and then to export results to molecular modeling software that can then take into the account quantum-level properties and behaviors of observed molecules, such as electronic orbital-electric field interactions.

All of the current simulations,<sup>6,11–14</sup> including one presented here, assume uniform material properties. However, in real experimental measurements, the materials at nanoscale may be highly heterogeneous, including nonidealized structures of the nanoparticles with sharp corners and points and rough surfaces

at molecular or higher scales. The simulations of the sharp metallic tips at different shapes in this work, as well as in other simulations,<sup>6,11–14</sup> suggest that the field distribution will be highly concentrated at the sharp corners and the points. For example, recent reports<sup>6,27</sup> have discussed the influence of triangular model-particle sharpness on the Raman enhancement. Particles with very sharp edges behave like point field enhancers. If the edge is immediately under the tip, the total electric field and Raman signal will be enhanced and the signal-to-noise ratio will be more favorable, giving a better compositional resolution. However, the spatial resolution will suffer in a case when the two-point field enhancer is presented within the diffraction-limited laser focal spot, and the decrease in resolution will be relative to the distance between the field enhancement induced by the tip and the field enhancement produced by the very sharp edge of the metallic particle. Thus, the influence of sharpness on the experimental AFM tip-enhanced Raman scanning microscopic measurements would be either to increase or to decrease spatial resolution and contrast, depending on the exact nanoscale structures of the nanoparticles. On the other hand, the simulated particles in this example have perfect boundaries. It is well-known that the surface roughness of the electrodes contributes to the enhancement of the SERS signal. Therefore, it is to be expected that a higher enhancement factor can be expected from a real particle with a rough surface. Furthermore, the nonuniform refractive index gradient, nonspherical geometry, multiple-particle clusters, and diffraction-limited Gaussian laser intensity distribution can significantly alter the calculated local electromagnetic field enhancement profile. Although an FEM simulation can incorporate some of this level of complexity into the simulation if proper material constants are introduced into the model, this is beyond the scope of this work. However, an AFM-SERS experiment and FEM simulation of more realistic scenarios are under development and will be reported elsewhere.

The main computational limitation, as in any method of solving a potential problem with a finite sized integration domain, is in selecting the proper model integration volume

space, boundary conditions, and mesh density. In any simulation of potential problems with an increase in size of the modeled space and mesh density, there is a dramatic increase in computing resource requirements. The finite element method has a significant advantage over the finite difference method in having nonuniform element sizes and locally enhanced mesh densities. Nonetheless, the computational requirements for complex geometric arrangements can still be a limiting factor. One of the ways to avoid this limitation is to carefully optimize mesh, with an increase in mesh density only in an area of interest, and a simultaneous decrease of mesh density near boundaries. For near-field calculations in nanotechnology, the mesh should typically have a density of at least 10–15 elements per unit of excitation wavelength, to avoid integration artifacts. The modeled volume should be created so that the boundaries are positioned far away from and do not interfere with the solution of the electromagnetic field distribution in the area of interest. The density of the element mesh should be maximal at the area of interest and then gradually decrease as the model approaches boundaries. In the case of Raman enhancement ( $E^4$ ), small variations in the electric field intensity will generate very high variations in the Raman signal. Therefore, it is imperative to have a saturated mesh density, i.e., to reach the optimal point of mesh volume and density where a further increase in each will not significantly change the calculated results. Sometimes, when having a very robust model requires a huge amount of computational resources, one option is to use symmetry constraints to reduce computational requirements.

## Conclusions

We demonstrate the use of frequency-domain, three-dimensional, finite element simulation in evaluating optimized configurations in AFM-SERS microscopy experiments. We have obtained maximum field-enhancement volume sizes that are in the same scale as observed spatial resolution of near-field optical confocal imaging techniques, i.e., about 20 nm.<sup>2,3</sup> Besides being useful for AFM-SERS studies, these results can be used to predict the signal enhancement in similar systems, for example, second harmonic generation microscopy techniques with metallic nanoparticle field enhancement.<sup>26</sup>

The high electric field enhancement has been calculated for a configuration of a single nanoparticle with the tip positioned above and irradiated horizontally with a laser beam. In the case of two adjoining nanoparticles, the electric field enhancement volume is constrained to the interstitial site, and the enhancement intensity can be as high as 165, which translates to a Raman signal ( $E^4$ ) enhancement of  $10^8$  to  $10^9$ . Besides contributing to the field enhancement, the tip plays a significant role in electric field polarization and locking in favorable geometric modes of field enhancements. The results of our FEM simulation lead to the following conclusions:

1. The tip apex diverging angle is not a critical limiting factor for achieving high field enhancement in AFM-SERS experiments. Therefore, a significant experimental effort to make a certain shape of AFM tips, which often requires sophisticated techniques, is not essential.
2. The field enhancement changes by only a factor of 2 when the nanoparticle size changes from 10 to 80 nm. Therefore, nanoparticle size inhomogeneity can be experimentally accepted in a wide range.
3. The 10-nm nanoparticle can still provide adequate field enhancement in AFM-SERS experiments, which can be used as probes in biological or other complex systems.
4. The difference in field enhancement exerted by the tip is not significant when it is positioned above a pair of geminal

nanoparticles. Field enhancement is mainly determined by the close proximity of the two nanoparticles, with the majority of the field enhancement intensity localized in the space between the nanoparticles. The factor controlling the field enhancement intensity is the particles' interstitial separation distance.

5. Also significant is the effect of the laser-beam propagation orientation angle relative to the tip axis. The intensity of the field enhancement rises significantly with the increase of the beam propagation angle toward 90°, as measured from the tip axes. The maximum field intensity is in the area where the vector of the electric field is parallel to the tip axis, which means that the vector of laser beam propagation is orthogonal to the tip axis. The tip mode-locking effect ensures that the enhancement volume shape and size do not change significantly for the wide range of angles, from 15° to 90°.

The simulation results presented here prove the concept of the high-resolution AFM-SERS experiments. Moreover, they show that by using smaller metallic nanoparticles, the system can map chemically complex environments such as cell membranes. The results may be used as a guide in designing physical experiments, by helping optimize conditions under which the highest enhancement and the highest resolution of the method will be achieved, with minimum trial and errors.

**Acknowledgment.** We thank Y. Martin and H. Wickramasinghe for their correspondence, G. Schenter and G. Holtom for their critical reading of manuscript, and S. Barlow and R. Brodzinski for helpful discussions. This work was supported by the Chemical Sciences Division of the Office of Basic Energy Sciences within the Office of Energy Research of the U.S. Department of Energy (DOE), and supported by the Laboratory Directed Research and Development Program of Pacific Northwest National Laboratory. The Pacific Northwest National Laboratory is operated by Battelle for DOE.

## References and Notes

- (1) Binning, G.; Quate, C. F.; Gerber, C. *Phys. Rev. Lett.* **1986**, 56, 930.
- (2) Paesler, M. A.; Moyer, P. J. *Near-Field Optics: Theory, Instrumentation and Applications*; John Wiley & Sons, Inc.: New York, 1996.
- (3) (a) Dunn, R. C. *Chem. Rev.* **1999**, 99, 2891. (b) Siku, H.; Dunn, R., C. *Anal. Chem.* **1999**, 71, 23A.
- (4) (a) Moskovits, M. *Rev. Mod. Phys.* **1985**, 57, 783. (b) Campion, A.; Kambhampati, P. *Chem. Soc. Rev.* **1998**, 27, 241. (c) Schatz, G. C. *Acc. Chem. Res.* **1984**, 17, 370. (d) Kim, W.; Safonov, V. P.; Shalae, V. M.; Armstrong, R. L. *Phys. Rev. Lett.* **1999**, 826, 4811. (e) Markel, V. A.; et al. *Phys. Rev. B* **1999**, 59, 10903.
- (5) (a) Kneipp, K.; et al. *Phys. Rev. Lett.* **1996**, 76, 2444. (b) Nie, S. C.; Emory, S. R. *Science* **1997**, 275, 1102. (c) Michaels, A. M.; Nirmal, M.; Brus, L. E. *J. Am. Chem. Soc.* **1999**, 121, 9932. (d) Bjerneld, E. J.; et al. *J. Phys. Chem. B* **2002**, 106, 1213. (e) Moyer, P. J.; et al. *J. Am. Chem. Soc.* **2000**, 122, 5409. (f) Michaels, A. M.; Jiang, J.; Brus, L. *J. Phys. Chem. B* **2000**, 104, 11965. (g) Eggeling, C.; et al. *J. Phys. Chem. A* **2001**, 105, 3673. (h) Fleischmann, M.; Hendra, P. J.; McQuillan, A. *J. Chem. Phys. Lett.* **1974**, 26, 183.
- (6) (a) Xu, H.; Bjerneld, E. J.; Käll, M.; Borjesson, L. *Phys. Rev. Lett.* **1999**, 83, 4357. (b) Xu, H.; Aizpurua, J.; Käll, M.; Apell, P. *Phys. Rev. E* **2000**, 62, 4318.
- (7) (a) Anderson, M. S. *Appl. Phys. Lett.* **2000**, 76, 3130. (b) Anderson, M. S.; Pike, W. T. *Rev. Sci. Instrum.* **2002**, 73, 1198.
- (8) Stockle, R. M.; Suh, Y. D.; Deckert, V.; Zenobi, R. *Chem. Phys. Lett.* **2000**, 318, 131.
- (9) (a) Hayazawa, N.; Inoue, Y.; Sekkat, Z.; Kawata, S. *Chem. Phys. Lett.* **2001**, 335, 183. (b) Hayazawa, N.; Inoue, Y.; Sekkat, Z.; Kawata, S. *J. Chem. Phys.* **2002**, 117, 1296.
- (10) Suh, Y. D.; Schenter, G. K.; Zhu, L.; Lu, H. P. *Ultramicroscopy*, in press.
- (11) (a) Krug, J. T., II; Sanchez, E. J.; Xie, S. X. *J. Chem. Phys.* **2002**, 116, 10895. (b) Bian, R. X.; Dunn, R. C.; Xie, X. S.; Leung, P. T. *Phys. Rev. Lett.* **1995**, 75, 4772.
- (12) Milner, R. G.; Richard, D. *J. Microsc.* **2001**, 202, 66.
- (13) Novotny, L.; Bian, R.; Xie, S. X. *Phys. Rev. Lett.* **1997**, 79, 645.

- (14) Martin, Y. C.; Hamann, H. F.; Wickramasinghe, H. K. *J. Appl. Phys.* **2001**, 89, 5774.
- (15) Courant, R. L. *Bull. Am. Math. Soc.* **1943**, 5, 1.
- (16) Silvester, P. P. *Alta Frequenza* **1969**, 38, 313.
- (17) Mackele, J. *Finite Elements Anal. Design* **2001**, 37, 575.
- (18) Sun, Y.; Bell, T.; Zheng, S. *Thin Solid Films* **1995**, 258, 198.
- (19) Johnson, P. B.; Christy, R. W. *Phys. Rev. B* **1972**, 6, 4372.
- (20) Ansys Multiphysics Theoretical Manual, <http://www.ansys.com>.
- (21) Verkeleij, A. J.; Leunissen, L. M. In *Immuno-Gold Labeling in Cell Biology*; Leunissen, J. L. M., Ed.; CRC Press: Boca Raton, FL, 1996.
- (22) Boyer, D.; Tamart, P.; Maali, A.; Louinis, B.; Orrit, M. *Science* **2002**, 297, 1160.
- (23) Kniepp, K.; Haka, A. S.; Kniepp, H.; Badziadegan, K.; Yoshizawa, N.; Boone, C.; Shafer-Peltier, K. E.; Motz, J. T.; Dasari, R. R.; Feld, M. S. *Appl. Spectrosc.* **2002**, 56, 150.
- (24) (a) Cho, K. *Prog. Theor. Phys. Suppl.* **1991**, 106, 225. (b) Cho, K.; Ohfuti, Y.; Arima, K. *Jpn. J. Appl. Phys.* **1995**, 34, Suppl. 34–1, 267.
- (25) Paule, E.; Reineker, P. *J. Phys. Chem. B* **2001**, 105, 4293.
- (26) (a) Clark, H. A.; Campagnola, P. J.; Wuskell, J. P.; Lewis, A.; Loew, L. M. *J. Am. Chem. Soc.* **2000**, 122, 1234. (b) Peleg, G.; Lewis, A.; Bouevitch, O.; Loew, L. M.; Parnas, D.; Linial, M. *Bioimaging* **1996**, 4, 215.
- (27) Kottmann, J. P.; Martin, O. J. F.; Smith, D. R.; Shultz, S. *Opt. Exp.* **2000**, 6, 213.